

The effects of an open and closed divertor on particle exhaust during edge-localized mode suppression by resonant magnetic perturbations in DIII-D

This article has been downloaded from IOPscience. Please scroll down to see the full text article.

2010 Nucl. Fusion 50 034011

(<http://iopscience.iop.org/0029-5515/50/3/034011>)

View [the table of contents for this issue](#), or go to the [journal homepage](#) for more

Download details:

IP Address: 198.35.2.237

The article was downloaded on 20/04/2010 at 16:37

Please note that [terms and conditions apply](#).

The effects of an open and closed divertor on particle exhaust during edge-localized mode suppression by resonant magnetic perturbations in DIII-D

E.A. Unterberg^{1,a}, O. Schmitz², T.E. Evans³, R. Maingi⁴,
N.H. Brooks³, M.E. Fenstermacher⁵, S. Mordijck⁶, R.A. Moyer⁶
and D.M. Orlov⁶

¹ Oak Ridge Institute for Science and Education, Oak Ridge, TN, USA

² Forschungszentrum Jülich GmbH, IEF4-Plasma Physics, 52428 Jülich, Germany

³ General Atomics, San Diego, CA 92186-5608, USA

⁴ Oak Ridge National Laboratory, Oak Ridge, TN, USA

⁵ Lawrence Livermore National Laboratory, Livermore, CA, USA

⁶ University of California-San Diego, La Jolla, CA, USA

E-mail: unterberge@fusion.gat.com

Received 16 May 2009, accepted for publication 10 November 2009

Published 23 February 2010

Online at stacks.iop.org/NF/50/034011

Abstract

This paper compares the effects of divertor geometry on particle exhaust characteristics during the suppression of ELM using resonant magnetic perturbations (RMPs) on DIII-D. The subject is timely, particularly for ITER, because the combination of techniques to control or mitigate ELMs and control particle exhaust can provide confidence in the ability of an external pumping system to fully remove the particle exhaust. The differences between an open and closed divertor magnetic topology show a strong coupling of the perturbed strikepoint to the pumping manifold in closed divertor configurations, which can increase the particle exhaust by a factor of four. There is also an observed dependence on q_{95} in this configuration, which is a common feature of RMP ELM suppression. Neutral density in both the active and non-active divertors is seen to increase during the RMP in the ISS configuration, and edge plasma conditions (i.e. $n_{e,sep}$ and midplane profile of D_{α}) are seen to increase in the closed divertor configuration. Finally, the pumping exhaust is also shown to have a strong dependence on local measurements of the recycling flux. These observations, when taken as a whole, point to a substantial change in the plasma edge conditions, i.e. near the LCFS, throughout the poloidal cross-section of the vacuum vessel. This is coincident with the application of the RMP affecting the pumping capability of the system.

PACS numbers: 28.52-s, 52.25.Fi, 52.25.Ya, 52.55.Dy, 52.55.Fa

(Some figures in this article are in colour only in the electronic version)

1. Introduction

The suppression of edge-localized modes (ELMs) using resonant magnetic perturbations (RMPs) on DIII-D has been extensively studied and reported on [1–5]. These studies have been carried out in a variety of cross-sectional shapes and edge collisionalities [4, 5]. In recent experiments, the cross-sectional shape (i.e. the averaged upper and lower triangularity, $\langle\delta\rangle$) and the edge collisionality, ν_e^* , [6] are nearly matched with those expected in ITER. These discharges are termed ITER

similar shaped (ISS) discharges [5], and have $\langle\delta\rangle \sim 0.55$ and $\nu_e^* \leq 0.2$. Past experiments had $\langle\delta\rangle \sim 0.3$ and $\nu_e^* \leq 0.2$. These are termed low- $\langle\delta\rangle$ discharges in this paper. Hardware modifications to the lower pump plenum baffle in DIII-D allow pumping of discharges with the higher $\langle\delta\rangle$ shapes (i.e. the ISS configuration). Recent reports note a wide variability in the core plasma particle loss during the RMP which depends on ν_e^* , $\langle\delta\rangle$, and possibly wall conditions with both configurations [7, 8]. Such variability leads to concerns of particle exhaust control during the RMP. For ITER in particular, combining techniques to control or mitigate the ELMs as well as control particle exhaust are of keen interest to provide confidence in

^a Author to whom any correspondence should be addressed.

the successful operation of this future tokamak. These are also of general concerns for any future devices because it could lead to the particle exhaust not being fully removed by an external pumping system (e.g. particle retention in the first wall).

Divertor configurations are known to have large effects on the particle exhaust [9]. In DIII-D, it has been shown that effects that alter the pumping and confinement of neutrals within the divertor include: (1) changes in the outer strikepoint (OSP) in relation to the cryopump plenum entrance, (2) the location and angle of incidence of the strikepoint on the divertor target and (3) the height of the X-point above the divertor target [10–12]. These effects lead to different particle exhaust characteristics as the SOL and divertor characteristics change in response, and are important in particle exhaust control for any fusion system.

This paper details the effects of different divertor configurations on neutral particle exhaust during RMP ELM-suppressed discharges in DIII-D. The next section (2.1) shows the exhaust differences between the low- and high- $\langle\delta\rangle$ discharges during RMP ELM suppression experiments on DIII-D. In this section, it is also shown how the magnetic topology of the active divertor leads to the changes in particle exhaust and can also lead to a high-recycling divertor in one configuration and a low-recycling divertor in the other. Then it is shown, in section 2.2, how plasma edge conditions change during the RMP in both configurations and the effects on pumping exhaust. Finally, section 3 gives a summary and conclusions on these results.

2. Characteristics of open and closed divertors during RMP application

A clear difference in the pumping capability during RMP ELM suppression of discharges with low- $\langle\delta\rangle$ versus ISS shapes is seen in DIII-D [8]. It is seen that the cryopumping system in ISS becomes the main particle sink, whereas in the low- $\langle\delta\rangle$ discharges the graphite walls are the dominant sink. This paper characterizes these phenomena and shows that optimizing the RMP magnetic configuration with respect to the divertor can lead to a situation where all the exhausted particles are removed by an external pumping system during the RMP.

2.1. Comparison of the pumping characteristics and magnetic topology

The analysis of the pumping characteristics is carried out using a single reservoir particle balance [7, 13]. The balance is given by $S_{\text{wall}} = S_{\text{IN}} - S_{\text{OUT}} - dN_p/dt$ where S_{IN} is the total particle input rate (i.e. $S_{\text{NBI}} + S_{\text{gas}}$); S_{OUT} is the rate of particles which are lost from the system. It comprises both S_{cryo} , the divertor pump exhaust rate, and dN_0/dt , the rate of neutral particle buildup, which is negligible when the cryopumping system is active. Finally, dN_p/dt is the derivative of the core plasma particle content. This balance assumes, first, that all the core plasma particles are completely D_2 which is generally confirmed by Z_{eff} measurements in both configurations [5, 14], and, secondly, that all unaccounted for particles are absorbed by the graphite wall in DIII-D. It is also noted that all the quantities except the remainder, S_{wall} , are measured quantities [13].

The results of this calculation for both configurations are shown in figure 1. As can be seen in figures 1(a) and (b) there is a substantial drop in the total number of particles in the core, N_p , when the RMP is applied at 2 s. This drop can be up to $\sim 30\%$ in some discharges [7]. In both discharges the particle input rate is the same, i.e. $\sim 4\text{--}8 \times 10^{21}$ particles s^{-1} , in the L-mode phase (< 0.75 s) and drops to $\sim 1 \times 10^{21}$ particles S^{-1} during the H-mode transition and stays at this level throughout the remainder of the discharge. Furthermore, during the RMP phase the particle exhaust, S_{cryo} , increases between the two configurations by 50% near the initiation of the RMP at $t \sim 2$ s and to nearly 100% at $t \sim 4$ s (figures 1(e) and (f)). Figures 1(g) and (h) show the distance from the OSP, R_{OSP} , to the opening of the pumping plenum baffling, R_{BAF} . This distance is given by $\Delta_{\text{BAF}} = R_{\text{OSP}} - R_{\text{BAF}}$ which is known to affect the pumping characteristics in DIII-D [10]. Here the ISS shape has a strikepoint ~ 2 cm closer to the pump plenum opening during the RMP, i.e. $\Delta_{\text{BAF}} \sim 4$ cm in the ISS case to $\Delta_{\text{BAF}} \sim 6$ cm in the low- $\langle\delta\rangle$ case. Figures 1(i) and (j) show the calculated remainder term of the balance, S_{wall} , termed the wall loading rate. This shows there is a large wall loading rate in the L-mode phase, but during the H-mode the rate is near zero. There is also seen a strong burst of particles during the initiation of the RMP, but after ~ 100 ms the rate either goes back to zero in ISS or stays high ($\sim 1 \times 10^{21}$ particles s^{-1}) for the low- $\langle\delta\rangle$ shape. The transient burst of particles at the initial turn-on of the coils is thought to be associated with the limited conductance of the cryo-system. If the conductance of the baffling system was high enough, it is thought there would be no transient increase as the cryopump would then be able to handle such high particle rates. Finally, the time integral of wall loading rate, N_{wall} , $N_{\text{wall}}(t) = \int_0^t S_{\text{wall}} dt'$, is shown in figures 1(k) and (l). Here it can be seen that the increase in S_{wall} leads to a strongly increasing wall inventory during the RMP phase ($t \geq 2$ s) in low- $\langle\delta\rangle$ and a much lower wall inventory increase in ISS during this phase. Beyond an initial change in the core particle content which affects the global balance in L-mode, the main difference between the two configurations is the exhaust rate during the RMP (figures 1(e) and (f)). This leads to a wall inventory buildup of $\sim 50\%$ during the RMP in the low- $\langle\delta\rangle$ shape as seen in figure 1(l), which is in contrast with only a slight change in the wall inventory for the ISS configuration, as seen in figure 1(k). From this analysis alone, one simple conclusion is that Δ_{BAF} decreased and therefore the exhaust rate increased which in turn led to the reduction in S_{wall} during the RMP phase of the ISS discharge. Indeed, such a conclusion neglects the applied asymmetries due to the RMP coils on the particle exhaust, but on the other hand, previous work to develop the first flight neutral model which the Δ_{BAF} formalism is part of neglected asymmetries due to error fields [10].

To quantify whether Δ_{BAF} is indeed the largest contributor to the pumping difference, the RMP ‘sink ratio’ is calculated. This ratio is given as $\Delta N_{\text{wall}}/\Delta N_{\text{cryo}}$ where N_{cryo} is the time integral of the total pumping exhaust from all cryopumps in DIII-D and Δ denotes a time domain from the beginning of the RMP phase until the perturbation is deactivated. Therefore in this context it denotes the relative change in particle content of either the wall, N_{wall} , or the particle exhaust, N_{cryo} , during the RMP. A database of all low- v_e^* (≤ 0.2) RMP discharges with

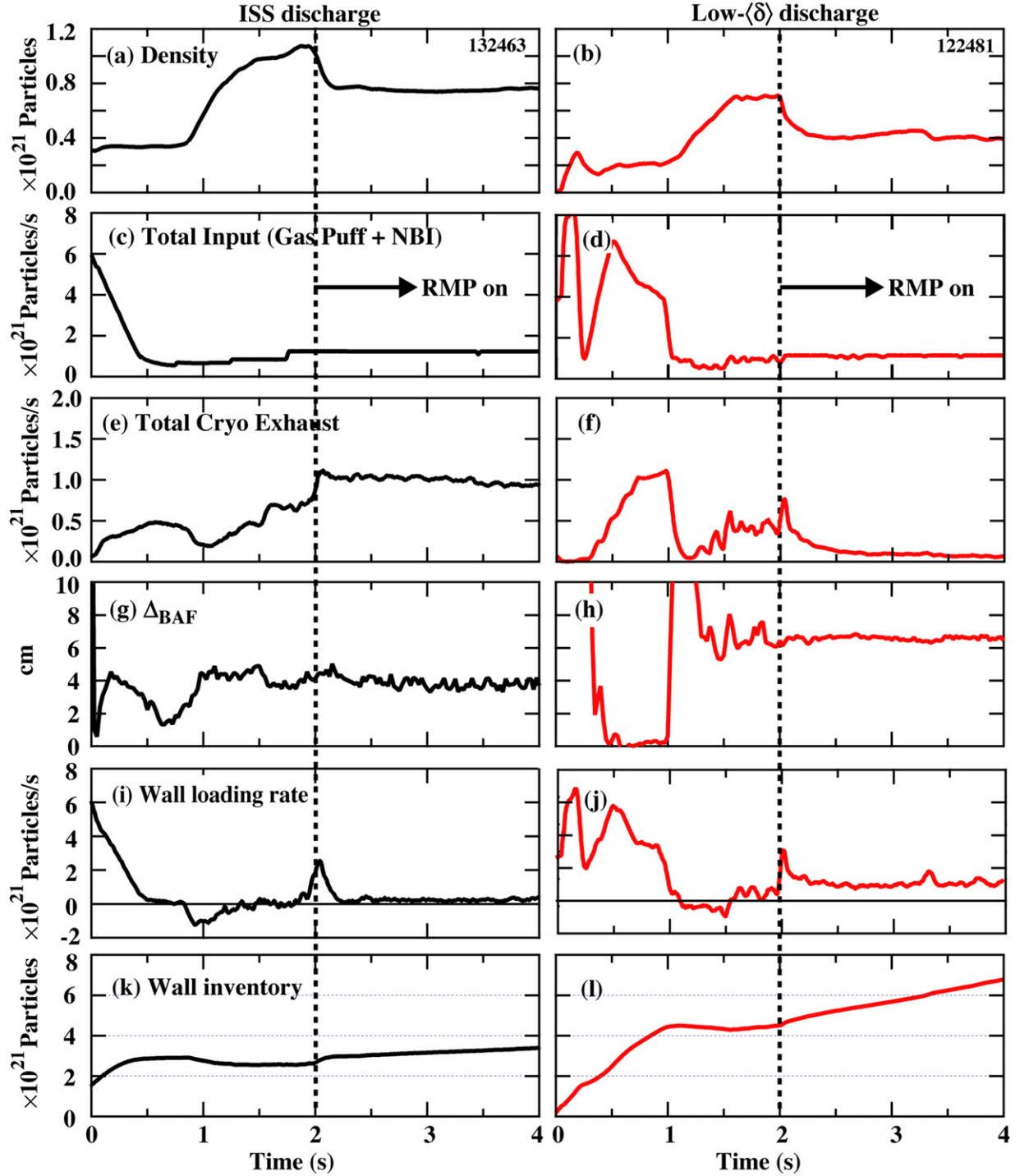


Figure 1. Details of the single reservoir particle balance for the two configurations under consideration, ISS and low- $\langle\delta\rangle$. (a) and (b) give the core particle content, N_p ; (c) and (d) give the total particle input rate, S_{IN} , considering both the gas puff and NBI fuelling; (e) and (f) give the total exhaust rate, S_{cryo} ; (g) and (h) give the distance for the OSP to the pump plenum entrance, Δ_{BAF} ; (i) and (j) give the calculated wall loading rate, S_{wall} , and (k) and (l) give the time integral of the wall loading rate, the wall inventory.

ELM suppression was compiled and compared with Δ_{BAF} of each discharge, and the results are shown in figure 2. The average value and deviation for each cross-sectional shape are also shown to give trends. The average values are $\Delta N_{wall}/\Delta N_{cryo} \sim 1$ and $\Delta_{BAF} \sim 3.75$ cm in the ISS shape and $\Delta N_{wall}/\Delta N_{cryo} \sim 4.5$ and $\Delta_{BAF} \sim 5$ cm in the low- $\langle\delta\rangle$ shape. The relatively small spread in the $\Delta N_{wall}/\Delta N_{cryo}$

value in the ISS shape versus the low- $\langle\delta\rangle$ shape should be noted. In each case there is ~ 1 – 1.5 cm deviation in Δ_{BAF} . The difference in this average RMP sink ratio is consistent with the approximate four times increase in the pumping rate in each case shown earlier, but there is no apparent correlation with a decreasing sink ratio as Δ_{BAF} decreases, which is expected if the ΔN_{cryo} term was increasing (i.e. more pump exhaust as

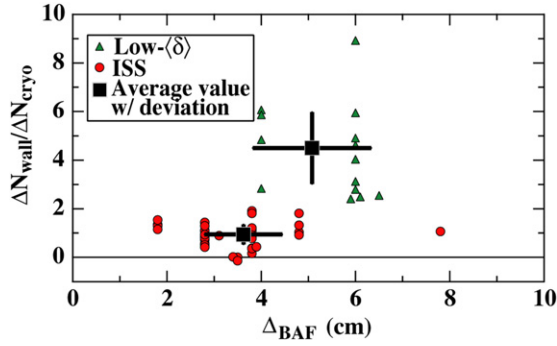


Figure 2. Database plot of the sink ratio, $\Delta N_{\text{wall}}/\Delta N_{\text{cryo}}$, versus the distance from the calculated equilibrium strikepoint, Δ_{BAF} in both the low- $\langle\delta\rangle$ and ISS configurations. The averages and deviations from those averages of each database are also shown in order to show the trend.

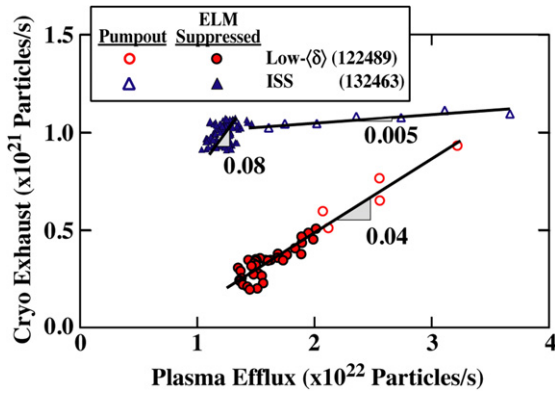


Figure 3. The measured cryopump exhaust versus an estimated plasma efflux for both configurations. A wall recycling coefficient of 0.95 was used to estimate the plasma efflux.

the OSP approached the plenum opening). This leads one to believe that this simple analysis is too optimistic and the 3D nature of the OSP during the RMP should be accounted for. Such an analysis is discussed later in this section.

Furthermore, pumping by the wall and the cryopumps has different characteristics: (1) during the RMP, (2) between the shapes and (3) within the RMP phase of the ISS shape itself. Figure 3 shows the pumping exhaust rate, S_{cryo} , versus the plasma efflux during the RMP phase for two representative discharges. Here the plasma efflux is defined as $N_{\text{TOT}}/[\tau_p^* \cdot (1 - R)]$, where N_{TOT} is the number density of the core plasma, τ_p^* is the effective confinement time ($=N_{\text{TOT}}/[S_{\text{IN}} - dN_{\text{TOT}}/dt]$) and R is the recycling coefficient. Since R is not measured in DIII-D and is dependent on incident particle energy and flux, an effective R is assumed to be 0.95. This value was chosen by taking a weighted average of recent calculations of a spatially resolved R for a typically LSN DIII-D discharge [15]. Information on the fraction of particle exhaust that is removed by the cryopumps can be obtained by fitting a line to the particular data set. This line is given by $S_{\text{cryo}} = (\varepsilon_{\text{pump}} \cdot \text{Efflux}) + C_{\text{pump}}$, where the slope of the line, $\varepsilon_{\text{pump}}$, is considered the fraction of particles removed by the pumps or the cryopump efficiency and C_{pump} is an offset constant for the line. In the ELM-suppressed phase of the ISS discharges $\varepsilon_{\text{pump}} \sim 8\% \pm 0.5\%$, but in the pumpout phase $\varepsilon_{\text{pump}} \sim 0.5\%$. Here, the ‘pumpout phase’ is the time in the

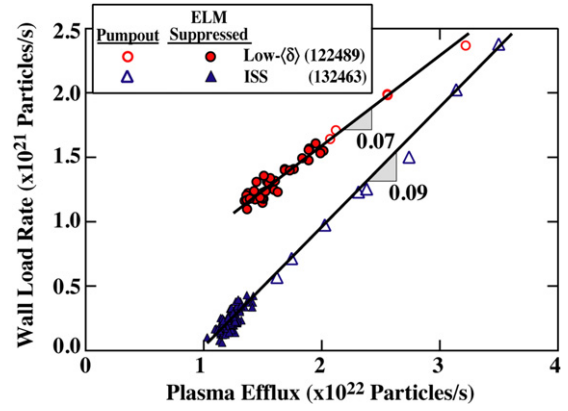


Figure 4. The calculated wall loading rate from the single reservoir particle balance versus the estimated plasma efflux for both coefficients. Again, the wall recycling coefficient was estimated to be 0.95 for the efflux estimate.

discharge when the density drops due to the initial turn-on of the perturbation coils. It is generally the first ~ 100 – 200 ms after the RMP coil is activated (e.g. see figures 1(a) or (b)) at $t \sim 2$ s. This is in contrast to the low- $\langle\delta\rangle$ case which is independent of the RMP phase with only a single $\varepsilon_{\text{pump}}$ of $\sim 4\% \pm 0.5\%$. Therefore, the measured pumping efficiency is about twice as high as in the ISS shape when compared with the low- $\langle\delta\rangle$ shape, which is similar to the results shown in figures 1 and 2. Although these results are highly dependent on R , this is thought to be a conservative estimate of the pumping efficiency and is consistent with other measurements. It is acknowledged that the uncertainty could be improved by direct measurements or particular modelling of the wall flux during the RMP as done in [15]. A similar fit to the data can be performed by replacing S_{cryo} with S_{wall} in the characteristic line formula and gives the wall pumping efficiency, $\varepsilon_{\text{wall}}$, which is a measure of the fraction of plasma efflux trapped in the graphite walls. Figure 4 shows the wall pumping efficiency for the same shots, $\varepsilon_{\text{wall}} (=S_{\text{wall}}/\text{Efflux} + C_{\text{wall}})$, where S_{wall} is the wall loading rate and C_{wall} is the offset constant). Here the $\varepsilon_{\text{wall}} \sim 7$ – 9% and does not change in the pumpout phase of the ISS. As expected, the wall pumping in these discharges is independent of the divertor geometry. Most surprising from this analysis is the large change in the $\varepsilon_{\text{wall}}$ term during the pumpout phase in the ISS shape but not in the low- $\langle\delta\rangle$ shape. This seems to point to a gross change in pumping and divertor conditions between the two configurations.

To investigate the 3D magnetic topology in the divertor region, the connection length of the field line, L_c , is calculated using the TRIP3D code [16, 17]. TRIP3D employs only the vacuum field calculation of the plasma equilibrium fields, external confining fields and the error fields in the system; as such there is no self-consistent calculation of the plasma response. Figure 5 is a poloidal-view contour plot of L_c around the X-point region of the plasma for both shapes. The splitting of the strikepoint, which is a common feature in the divertor region of RMP discharges, is evident [17, 18]. In each panel, the pump plenum baffle is shown as a ledge in the lower right-hand corner and the plenum entrance is represented by the notch below this baffle shelf. Another feature is how the strikepoint splitting is coupled to the baffle and plenum

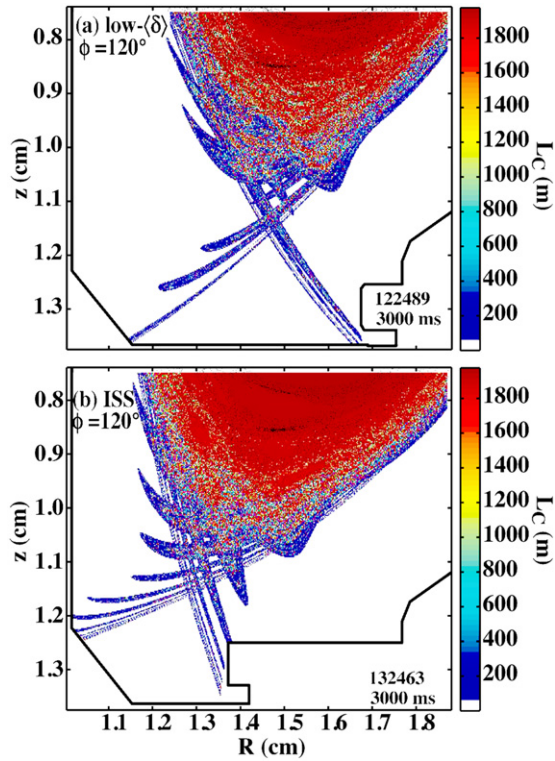


Figure 5. The poloidal view of the connection length calculation using the TRIP3D code in the divertor region for (a) the low- $\langle\delta\rangle$ and (b) the ISS configuration. Superimposed is the first wall boundary, and this boundary shows the change in the pumping baffling between the low configuration.

entrance. In the low- $\langle\delta\rangle$ case (figure 5(a)), the perturbed strikepoint is only interacting with the divertor target plates and not with the baffle nose or top shelf. Conversely, in the ISS shape (figure 5(b)), the perturbed strikepoint interacts not only with the target but also with the nose and the top shelf of the baffle. In this context, the divertor is said to be open in the low- $\langle\delta\rangle$ case because neutrals can easily escape into the main chamber from the divertor region after interacting with the target area [9]. In the ISS divertor, the perturbed strikepoint acts as a plasma ‘plug’ for the divertor and presumably keeps neutrals from easily escaping the divertor area. The fact that there are interactions with the top of the baffle shelf leads to other complications that will be addressed later in this paper.

The same L_c calculations can also be projected toroidally into the divertor target and top shelf of the baffling. Figure 6 gives L_c plotted versus toroidal angle and the distance to the baffle entrance given in a percentage from the calculated asymmetric strikepoint where 0% is at this ‘unperturbed’ strikepoint location, 100% is the pump plenum entrance and $>100\%$ is on the baffle nose or the top shelf. The area between 0% and 100% is the region that would give a closed or open divertor when the axisymmetric strikepoint is perturbed. This relative scale is used to make a direct comparison easier between the two configurations due to the large absolute scale difference as a result of the baffle modifications mentioned earlier. Qualitatively, it can be seen that the ISS shape (figure 6(b)) has much more short L_c field lines incorporating this area than does the low- $\langle\delta\rangle$ shape (figure 6(a)). Quantitatively, the area covered by short L_c in

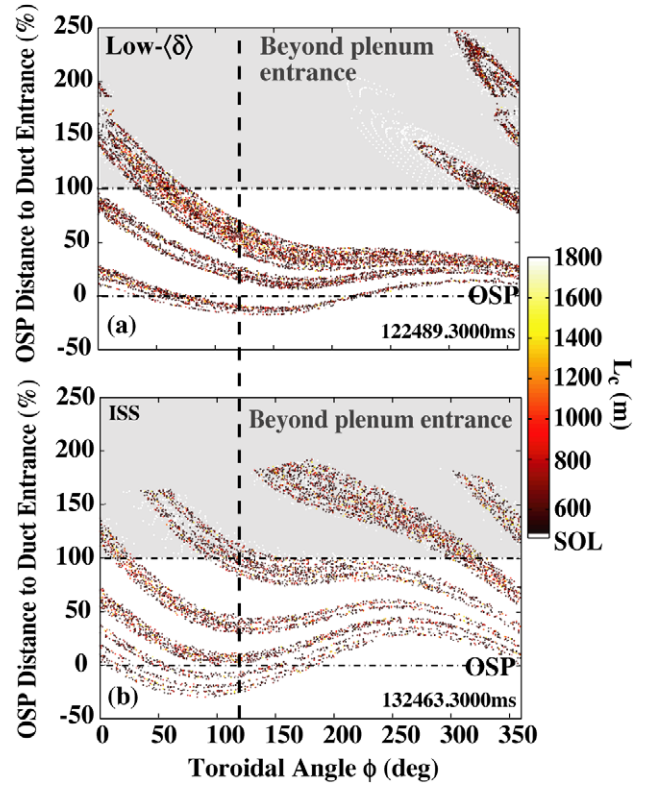


Figure 6. The toroidal view of the connection length calculation using the TRIP3D code in the divertor region for (a) the low- $\langle\delta\rangle$ and (b) the ISS configuration. The OSP is labelled by a horizontal dashed line in both sub-panels. A vertical line at $\phi = 120^\circ$ shows the location of the poloidal cut shown in figure 5. The dashed line at 100% gives the location of the pump entrance in both sub-panels.

a region in front of the baffle entrance has $a \sim 0.55$ coverage fraction for the ISS shape and ~ 0.22 coverage fraction in the low- $\langle\delta\rangle$ shape. These fractions are estimated by taking the toroidal angle in front of the plenum entrance that is ‘covered’ by short L_c field lines and dividing that by the full toroidal circumference. Therefore following the argument for dependence of plenum pressure on R_{OSP} given in [10], the neutral flux into the pump plenum is dependent on (1) the magnetic field structure, (2) the probability of re-ionization of neutrals within the gap between the OSP and the plenum entrance and (3) the flux of ions to the divertor floor. If re-ionization of neutrals were to be the dominant process, one would expect the neutral pressure to decrease. On the other hand, there could be a substantial change in either the ion flux to the floor or the magnetic incidence angle both of which would change the neutral pressure in the plenum.

Figure 7 shows the pumping efficiency, ε_{pump} , and wall efficiency, ε_{wall} , versus the q_{95} of the plasma. In this particular shot, the baseline ε_{pump} is $\sim 2\%$ (figure 7(a)) when the RMP is applied, and the ε_{wall} baseline during the RMP is $\sim 3\%$ (figure 7(b)), which is $\sim 1/2$ that shown in figure 4. As the q_{95} approaches discrete values, shaded in grey in the figure, large deviations in the pumping efficiency can be seen (up to 6–9% which is the same efficiency shown in figure 3). It should also be noted that the wall efficiency drops to negative, or near negative, values, which implies there is particle released from the wall at these q_{95} values. The transient

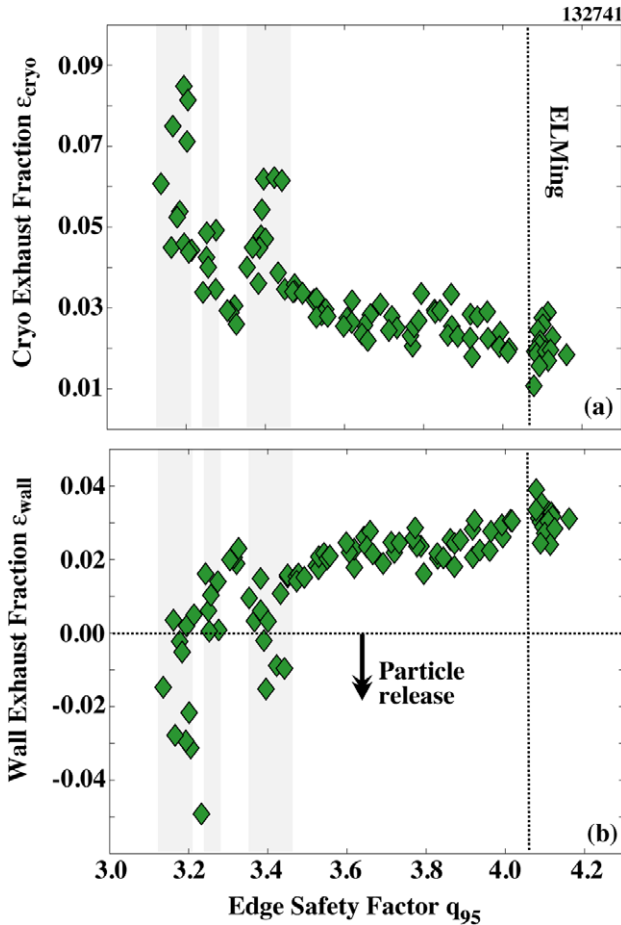


Figure 7. Both the cryopumping efficiency (sub-panel a) and the wall pump efficiency (sub-panel b) for an ISS configuration as a function of q_{95} . The shaded regions at $q_{95} \sim 3.4$ and 3.2 are the RMP resonance locations.

increases in the pumping efficiency are thought to be linked to the perturbed strikepoint, as shown in figure 6, and the change in this perturbed strikepoint as these footprint lobes move and couple to the pumping manifold. These pumping fluctuations correlated with discrete q_{95} ranges are consistent with variations in the electron temperature [19] and in the particle flux profile to the divertor target [17, 20] reported on earlier. This modulation in both efficiencies is a further indication that the magnetic topology is affecting the pumping.

2.2. Characteristics of the SOL and neutral pressure during the RMP

Upstream conditions, i.e. ‘upstream’ of the divertor target if one follows a SOL flux tube, can also significantly contribute to the divertor (downstream) conditions. Typically, midplane profiles are used as proxies for the upstream conditions. Figure 8 shows the analysis of an ISS discharge upstream profiles of electron density and temperature, and D_{α} intensity. These profiles are used to determine the SOL conditions during the RMP phase of the discharge. Figures 8(a) and (b) give time histories of the line-averaged density and lower divertor D_{α} intensity as a reference. A vertical line is drawn at two times (2 s and ~ 3 s, labelled ‘1’ and ‘2’ respectively) to show

when the subsequent profiles are taken. Figure 8(c) gives the D_{α} intensity profiles for the two time slices. Here it can be seen that in the RMP case the D_{α} intensity is much higher than in the ELMy H-mode phase, even beyond the last closed flux surface (LCFS). This increase in photon flux is an indication of increased plasma or neutral particles in the SOL [21]. Coupled with the SOL plasma parameters of electron density, n_e (figure 8(d)), and electron temperature, T_e (figure 8(e)), one can deduce the neutral particle density [22], but this is not done here. Nevertheless, this increase in intensity is indicative of increased neutral flux in the near SOL and corroborates the ionization gauge measurements shown in the next figure (figure 9).

Such large changes in the SOL have a profound effect on the plenum pressure and pumping speed of the cryopump. The difference in pumping is exemplified in the total pressure in the cryopumping plenum during the RMP in both shapes. Figure 9 shows the pressure in the pump plenum for an ISS (dashed line) and low- δ shape (solid line) during an RMP discharge. The plenum pressure is measured by ionization gauges adapted to work in high magnetic fields [23]. The pressure is directly related to the pumping speed of the cryopump and, therefore, indicates the particle uptake by the particular pump. It should be noted that the recent modifications made in the lower pump plenum baffle do not change the conductance of the plenum, and therefore, the change in pumping is not due to this possibility [5, 8]. In this figure, the pressure matches in these two cases just before the RMP is applied ($t = 2$ s.), disregarding the variations earlier in the discharge ($t = 0$ – 1.5 s). During the RMP ($t > 2$ s.), the pressure in shot 123301 (solid line) drops exponentially while in shot 134162 (dashed line) the pressure stays at a higher value than even before the RMP was applied. These pressure traces are typical of each shape and are attributed to the divertor geometry and changes in the SOL characteristics.

Divertor pumping and closure are also characterized by how the plenum pressure changes as the line-averaged density or separatrix density increases. Generally, these characterizations show that the higher the slope the more closed the divertor is said to be [9, 24]. Figure 10 compares how the plenum pressure changes with respect to the separatrix electron density for a time interval during the non-RMP ELMy phase (full symbols) as well as the RMP ELM-free phase (open symbols). The separatrix density, $n_{e,sep}$, is deduced from the value of a hyperbolic tangential fit to the Thomson scattering radial profile taken at the LCFS [25]. In figure 10, the separatrix density and plenum pressure are the same for both shapes before the application of the RMP. After the application of the RMP, the pressure in the plenum is seen to diverge, with the ISS case increasing in pump plenum pressure as the separatrix density decreases and the low- δ case decreasing as the separatrix density decreases. This bifurcation in the pump plenum pressure between the two configurations also implies a plasma plugging effect is taking place in the ISS case.

Similarly, the plenum pressure versus the D_{α} intensity was plotted in figure 11 to give an indication of the change in the recycling flux at both the outer strikepoint, OSP, (figure 11(a)) and the inner strikepoint, ISP, (figure 11(b)) locations. This was done to determine whether the neutral pressure increase or decrease in the SOL and pump plenum can be correlated

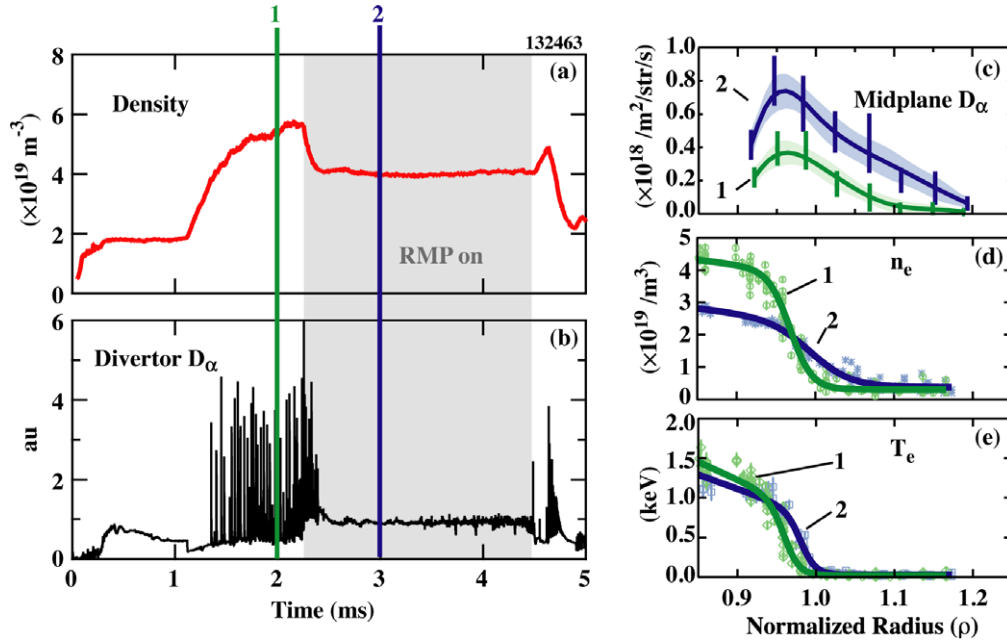


Figure 8. Time histories of the line-averaged density (a) and divertor D_α for reference. The vertical lines labelled ‘1’ and ‘2’ denote when radial profiles of the midplane D_α (c), electron density (d) and electron temperature (e) were taken.

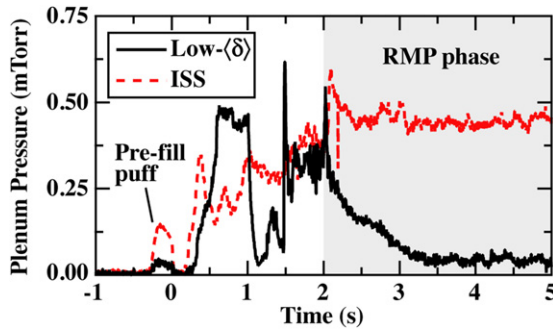


Figure 9. A comparison of the pressure time history in the pump plenum between the two configurations. Shot 123301 gives a typical low- $\langle\delta\rangle$ configuration trace and shot 134162 gives a typical ISS trace. The RMP phase is shaded in grey.

with an increase in recycling flux due to the RMP. These plots are for times only with an RMP applied and do not include times during the ELMy phase. Here it can be seen that in the ISS case, the recycling light and plenum pressure stay high near both the ISP and OSP, and the pressure slightly increases with D_α intensity. In the low- $\langle\delta\rangle$ case, the recycling light is typically two times lower in the OSP when compared with the ISS case, and the recycling light and plenum pressure exhibit a near linear relation when the latter is below ~ 0.3 mTorr. At the ISP, the D_α intensity is about four times the ISS intensity and falls to zero over the RMP phase of the discharge. Both of these figures indicate that the plenum pressure seems to be following the recycling flux, i.e. as the flux decreases the pressure in the plenum decreases as well, and suggests that neutral recycling could be the main driver for the pumping pressure and the edge plasma conditions. It should also be noted that in the low recycling divertor (i.e. the low- $\langle\delta\rangle$) there is strong evidence the divertor goes into a conduction limit regime, which was explained in detail in [14].

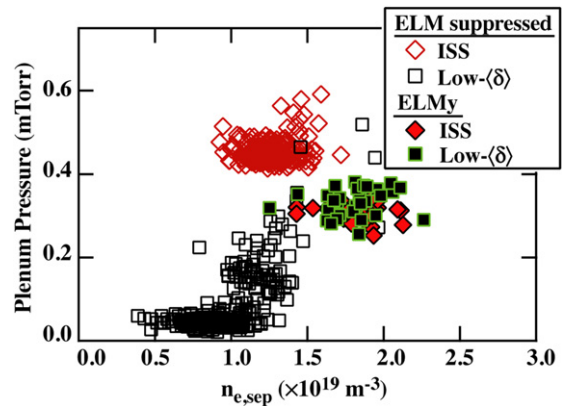


Figure 10. Plenum pressure versus separatrix electron density. Both configurations are plotted as are data points in the ELMy regime of each discharge for comparison within as well as between configurations.

As shown in figures 11(a) and (b), the increase in the recycling light is coincident with an increase in plenum pressure. A more detailed look at the neutral pressure in the pump plenums is shown in figure 12. Here it is seen that the main contribution to the increase in pressure is from the lower outer cryopump (figure 12(a)), as would be expected from a lower-single-null (LSN) plasma on DIII-D. A closer inspection of the pressure in the upper (non-active) divertor region reveals that while the pressure initially increases during the first application of the RMP, it is more than 100 times smaller than the lower outer cryopump. The slow increase in pressure later in time, seen in figure 12(b), is not yet understood, but is indicative of transient changes in the SOL and/or main chamber wall recycling during the RMP, and the trend up in neutral density throughout the poloidal cross-section of the SOL is consistent with spatially resolved (in poloidal angle) observations of D_α intensity [8].

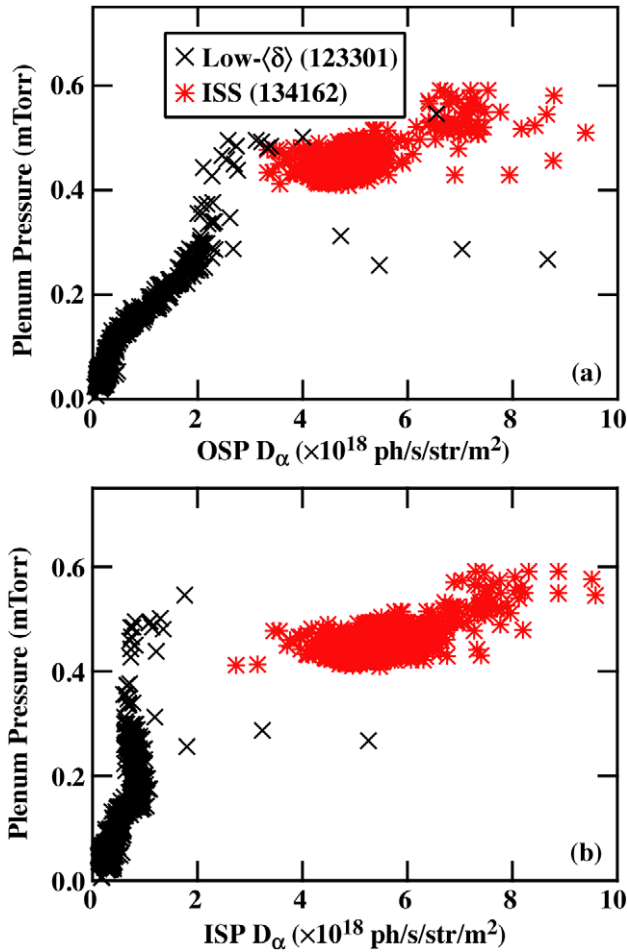


Figure 11. Plenum pressure versus D_α light intensity at both the OSP (a) and the ISP (b) for both configurations during the RMP phase. Shot 123301 is the low- $\langle\delta\rangle$ configuration and shot 134162 is the ISS configuration. D_α intensity here is used as a proxy for recycled neutrals.

When the observations shown in the preceding paragraphs are taken together, they point to a substantial change in the plasma edge conditions, i.e. near the LCFS, throughout the poloidal cross-section of the vacuum vessel which is coincident with the application of the RMP. This change can be either beneficial, as in the ISS shape where the increased recycling leads to a higher exhaust rate, or detrimental, as is the case for the low- $\langle\delta\rangle$ configuration where the divertor falls into a low recycling, conduction limited regime [14].

3. Summary and conclusions

As has been described in a recent publication [8], the divertor configuration has pronounced effects on the particle exhaust during RMP ELM suppression in DIII-D. In this paper, we have shown more details of this phenomenon, particularly in the calculations of the magnetic topology and details of the SOL. In simulating the 3D divertor magnetic topology, the perturbed strikepoint is shown to couple extremely well to the pumping manifold in the ITER similar shape (ISS) and leads to an approximately four times increase in the pumping capability when compared with low- $\langle\delta\rangle$ shapes regardless of

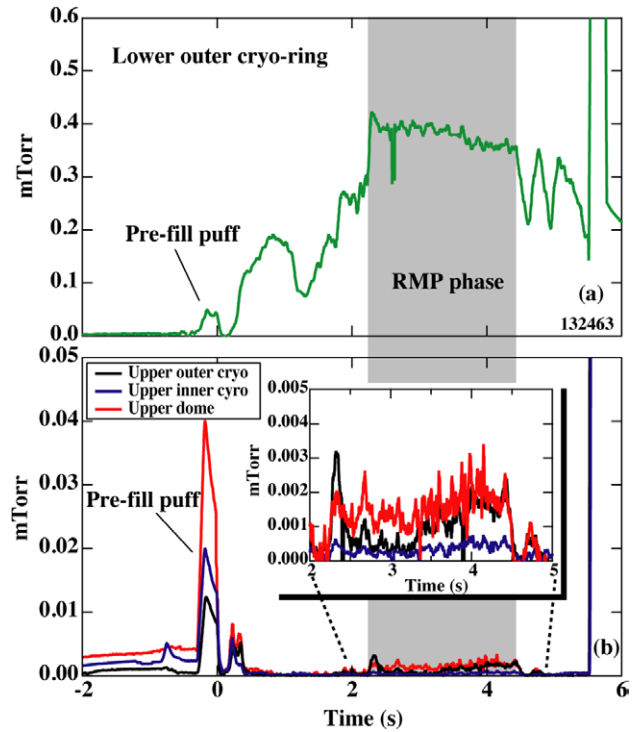


Figure 12. Time history of the pump plenum pressure for the lower divertor pump plenum (a) and the upper divertor region (b). The upper divertor has a cryopump on both the ISP side, labelled ‘upper inner cryo’ in the plot, and the OSP side, labelled ‘upper outer cryo’ in the plot. There is also a pressure gauge in the private flux region, labelled ‘upper dome’ in the plot.

the distance of the equilibrium strikepoint to the pump plenum entrance. The pumping efficiency of the cryopump is also seen to have specific ranges of q_{95} where the efficiency increased substantially. This feature has similarities with the resonant window seen for full ELM suppression using the RMP on DIII-D. The particle exhaust is observed to be coupled not only to the 3D magnetic topology but also to the wall recycling flux in ISS discharges whereas in the low- $\langle\delta\rangle$ discharges saw the recycling light go to zero during the RMP. The changes in the recycling during the RMP application are coincident with changes in the edge plasma conditions, namely $n_{e,sep}$ and radial D_α profile close to the LCFS. It is also coincident with increases in the cryopump plenum pressure with up to a four times increase in pumping capability when the magnetic topology is well aligned with the plenum entrance (i.e. comparing ISS divertor magnetic geometry with low- $\langle\delta\rangle$ geometry). To further the understanding of the changes to the SOL conditions during the RMP, modelling is currently underway using both 2D [SOLPS] and 3D [EMC3-EIRENE] edge fluid modelling [26, 27].

An optimal divertor magnetic topology that demonstrates both particle exhaust control as well as ELM suppression in DIII-D has been found at conditions similar to those of ITER, i.e. v_e^* , $\langle\delta\rangle$. This demonstration gives an initial indication that the RMP technique for suppressing ELMs is compatible with particle exhaust requirements for next-step devices such as ITER. Although a complete understanding is still missing, the importance of the 3D magnetic topology not only for the suppression of ELMs but also for particle control is apparent

and is reliant on the characterization of the edge plasma conditions. In general, the characterization of the particle exhaust and SOL conditions during the RMP are beneficial in giving a better understanding of the particle sources and sinks during the RMP, which will ultimately lead to more successful future RMP experiments.

Acknowledgment

This work was supported by the US Department of Energy under DE-AC05-06ER23100, DE-FC02-04ER54698, DE-AC05-00OR22725, DE-AC52-07NA27344 and DE-FG02-07ER54917. The first author is supported in part by the Magnetic Fusion Energy Postdoctoral fellowship from the Oak Ridge Institute for Science and Education.

References

- [1] Evans T.E. *et al* 2006 *Nature Phys.* **2** 665
- [2] Burrell K.H. *et al* 2005 *Plasma Phys. Control. Fusion* **47** B37
- [3] Moyer R.A. *et al* 2005 *Phys. Plasmas* **12** 056119
- [4] Evans T.E. *et al* 2005 *Nucl. Fusion* **45** 595
- [5] Evans T.E. *et al* 2008 *Nucl. Fusion* **48** 024002
- [6] Sauter O., Angioni C. and Lin-Liu Y.R. 1999 *Phys. Plasmas* **6** 2834
- [7] Unterberg E.A. *et al* 2009 *J. Nucl. Mater.* **390–391** 486
- [8] Unterberg E.A., Evans T.E., Maingi R., Brooks N.H., Fenstermacher M.E., Mordijck S. and Moyer R.A. 2009 *Nucl. Fusion* **49** 092001
- [9] Lorate A. 2001 *Plasma Phys. Control. Fusion* **43** R183
- [10] Maingi R., Watkins J.G., Mahdavi M.A. and Owen L.W. 1999 *Nucl. Fusion* **39** 1187
- [11] Klepper C.C., Hogan J.T., Hill D.H., Maingi R., Owen L.W., Buchenauer D.A., Mahdavi M.A. and Schaffer M.J. 1993 *Nucl. Fusion* **33** 533
- [12] Lasnier C.J., Hill D.N., Petrie T.W., Leonard A.W., Evans T.E. and Maingi R. 1998 *Nucl. Fusion* **38** 1225
- [13] Maingi R., Jackson G.L., Wade M.R., Mahdavi M.A., Mioduszewski P.K., Hass G., Schaffer M.J., Hogan J.T. and Klepper C.C. 1996 *Nucl. Fusion* **36** 245
- [14] Fenstermacher M.E., Evans T.E., Moyer R.A., Porter G.D., Boedo J.A., Burrell K.H., Groth M., Joseph I., Osborne T.H. and Watkins J.G. 2007 *J. Nucl. Mater.* **363–365** 476
- [15] Mioduszewski P.K. and Owen L.W. 2001 *J. Nucl. Mater.* **290–293** 443
- [16] Evans T.E., Moyer R.A. and Monat P. 2002 *Phys. Plasmas* **9** 4957
- [17] Schmitz O. *et al* 2008 *Plasma Phys. Control. Fusion* **50** 124029
- [18] Wingen A., Evans, T.E. and Spatschek K.H. 2009 *Nucl. Fusion* **49** 055027
- [19] Schmitz O. *et al* 2009 *Phys. Rev. Lett.* **103** 165005
- [20] Watkins J.G., Evans T.E., Jakubowski M., Moyer R.A., Schmitz O., Wingen A., Fenstermacher M.E., Joseph I., Lasnier C.J. and Rudakov D.L. 2009 *J. Nucl. Mater.* **390–391** 839
- [21] Colchin R.J., Brooks, N.H., Owen L.W., Maingi R., Isler R.C., Carlstrom T.N. and Groebner R.J. 2000 *Proc. 27th EPS Conf. on Controlled Fusion Plasma Physics (Budapest, Hungary)* vol 24B (European Physical Society) p 760 <http://epsppd.epfl.ch/Buda/pdf/p2-094.pdf>
- [22] Colchin R.J. *et al* 2000 *Nucl. Fusion* **44** 175
- [23] Hass G. and Bosch H.S. 1998 *Vacuum* **51** 39
- [24] Horton L. *et al* 1999 *Nucl. Fusion* **39** 1
- [25] Porter G.D., Moller J., Brown M., Lasnier C. and the DIII-D Team 1998 *Phys. Plasmas* **5** 1410
- [26] Mordijck S. *et al* 2009 *J. Nucl. Mater.* **390–391** 299
- [27] Frerichs H.E. *et al* 2009 Three-dimensional edge transport simulations for DIII-D plasmas with resonant magnetic perturbations *Nucl. Fusion* this issue